Compressed Sensing-Aided Index Modulation Improves Space-Time Shift Keying Assisted Millimeter-Wave Communications

Ibrahim A. Hemadeh, *Member, IEEE,* Siyao Lu, *Student Member, IEEE,* Mohammed El-Hajjar, *Senior Member, IEEE,* and Lajos Hanzo, *Fellow, IEEE*

***Abstract*—In this treatise, we present the concept of Compressed-Sensing (CS)-aided Space-Time Shift Keying Index Modulation (STSK-IM), where a virtual domain Orthogonal Frequency Division Multiplexing (OFDM) symbol is divided into N_a-sized blocks, which carry K STSK codewords over a specific combination of virtual-domain sub-carriers and then converted to the frequency domain with the aid of a CS matrix. We design the system for operation in the Milli-meter Wave (mmWave) frequency band. Furthermore, we amalgamate our soft-decision-aided scheme both with the concept of Coordinate-Interleaving (CI) as well as a Discrete Fourier Transform (DFT)-aided codebook design conceived for analogue beamforming, which is vitally important for mmWave systems. In the proposed system, the number of implicit bits conveyed by the activated sub-carrier Frequency Index (FI) is determined by the number of the available K to N_a sub-carrier permutations. Hence, we propose two FI allocation techniques, namely the Distinct FI (DFI) and the Shared FI (SFI) based schemes, which strike a trade-off between the attainable sparsity level and the achievable capacity limit. We then introduce a reduced-complexity detection technique in order to mitigate the detection complexity order of the optimum detector from $\mathcal{O}\left(N_c \cdot (Q \cdot \mathcal{L})^K\right)$ to $\mathcal{O}\left(\hat{N}_c \cdot (Q \cdot \mathcal{L})^K\right)$, where $\hat{N}_c \leq N_c$. We also formulate the Discrete-Input Continuous-Output Memoryless Channel (DCMC) capacity and invoke EXtrinsic Information Transfer (EXIT) charts for characterizing the achievable performance limit of the reduced-complexity aided detector. Finally, we analyze the BER performance of both the uncoded and of our coded CS-aided STSK-IM systems associated with both the optimum and the reduced-complexity detectors.**

***Index Terms*—Millimeter-wave communications, mmWave, 5G, Index modulation, Spatial modulation, Compressed Sensing, Coordinate Interleave, Reduced Complexity detection, wideband channel, channel coding, MIMO, Space-Time Shift Keying, Spatial Modulation, OFDM, PSK, QAM.**

The financial support of the EPSRC projects EP/Noo4558/1 and EP/L018659/1, as well as of the European Research Council's Advanced Fellow Grant under the Beam-Me-Up project and of the Royal Society's Wolfson Research Merit Award is gratefully acknowledged.

I. Introduction

The unprecedented wireless channel bandwidth potential of the Millimeter Wave (mmWave) band spanning from 30 GHz to 300 GHz [1], makes it attractive for future wireless standards [2], [3]. However, its high path loss [1] guided the research community towards adopting hybrid transceiver designs combined with sophisticated wideband techniques [4], [5]. Hybrid techniques combine digital and analogue components for mitigating the high path loss [4]. The digital component typically relies on a wide range of sophisticated Multiple-Input Multiple-Output (MIMO) techniques designed for striking a compelling multiplexing-diversity trade-off, as exemplified by Index Modulation (IM) systems [6]. By contrast, the Analogue Beamforming (ABF) component of the transceiver may rely on analogue circuitry-based Antenna Arrays (AAs).

In a nutshell, IM techniques [6] rely on a low-complexity On/Off mechanism in the time-, frequency-, or spatial-domain of wireless communications systems in order to implicitly convey the information mapped to the activated pattern of the components, together with the classic PSK/QAM symbols. To elaborate a little further, these components include a wide range of time, frequency and/or time dimension elements, such as the Antenna elements (AEs) [7], dispersion matrices [8], frequency sub-carriers [9], transmit Light Emitting Diodes (LEDs) [10], time slots [11] etc. Having them amalgamated with the mmWaves waveform, IM systems become capable of achieving improved data rates in next-generation networks [12]–[15].

To elaborate further, spatial domain IM techniques commonly include systems that invoke

space-assisted MIMO techniques. For instance, Spatial Modulation (SM) [7] constitutes one of the most popular IM techniques that has fascinated the community during the past decade. In SM, information is transmitted both over the classical PSK/QAM symbol as well as over the index of the activated transmit AE. This scheme was later generalized to activating multiple AEs, rather than just a single AE in the Generalized SM (GSM) scheme [16]. Additionally, SM was combined with Space-Time Block Coding (STBC) in the STBC-SM scheme [17] in order to attain a transmit diversity gain. Another SM-aided concept is referred to as Quadrature SM (QSM) [18], where the modulated PSK/QAM symbol is split into a real and an imaginary part to be transmitted on a specific pair of AEs. Various spatial domain IM techniques have already been introduced by the community into mmWave systems. For instance, Valliappan *et al.* [19] exploited the radiation pattern of the transmit AE sets in order to implicitly convey the activated radiation pattern index over mmWaves. Furthermore, an SM scheme based on a single RF chain was proposed by Yang *et al.* [20] for mmWave communications. Additionally, QSM was utilized by Younis *et al.* [18] for transmission over mmWaves.

The concept of SM was later extended to the frequency domain with the aid of an Orthogonal Frequency Division Multiplexing IM (OFDM-IM) scheme by Basar *et al.* [9]. In OFDM-IM, the sub-carriers available are partitioned into multiple blocks, where only a specific subset of sub-carriers is activated in each block to carry a selection of PSK/QAM symbols and to implicitly transmit the sub-carriers indices activated. Alternative waveforms were also used for frequency-assisted IM techniques, as exemplified by the non-orthogonal Generalized Frequency Division Multiplexing IM (GFDM-IM) system proposed by Ozturk *et al.* [21].

Another family of SM-inspired IM techniques is based on the dispersion matrix approach relying on the Space-Time Shift Keying techniques of Sugiura *et al.* [22]. In STSK, a single one out of many dispersion matrices - rather than AEs- is activated to disperse a single PSK/QAM symbol over both the spatial and time domains. This scheme was invoked for mmWave communications in the Layered Multi-Group Space-Time Shift Keying (LMG-STSK) system proposed in [23] as an amalgamation of STSK, Multi-User MIMO (MU-MIMO), beamforming and user grouping conceived for MU scenarios in the mmWavedownlink. Then it was amalgamated with the concept of Non-Orthogonal Multiple Access (NOMA) [24] in the Joint-Alphabet STSK (JA-STSK) approach [25] . The STSK scheme was later combined with the conventional SM in the Multi-Set STSK (MS-STSK) system of Hemadeh *et al.* [8] in order to transmit a single one out of many dispersion matrices over a specific combination of AEs, where the implicit index of the activated AEs is transmitted simultaneously with the STSK codeword. This scheme was later adopted for mmWave communications by relying on the LMG Multi-Set STSK (LMG-MS-STSK) scheme [15]. Furthermore, MS-STSK was also extended to the frequency domain in the Multi-Space-Frequency STSK (MSF-STSK) system [26], which is a sophisticated combination of OFDM-IM, MS-STSK and beamforming conceived for mmWave communications. The MSF-STSK scheme is capable of benefiting from the wide bandwidths available in the mmWave band for increasing the number of sub-carriers, hence increasing both the number of blocks as well as the number of bits per OFDM symbol.

The mmWave channel imposes a short delay spread of a few nanoseconds. In practice, short delay spreads are preferred, since they would require a short Cyclic Prefix (CP) for overcoming the Inter-Symbol Interference (ISI) imposed by the channel. However, given the high sampling rate required at such a high bandwidth, such as for example 1 GHz at a 500 MHz bandwidth in the 28 GHz frequency band the number of CP samples is still high. Nonetheless, it was shown in [23], [26] that a high number of sub-carriers per OFDM symbol can be used, hence the CP length is still tolerable.

To elaborate a little further, new MIMO signal processing techniques were proposed in the literature [27], [28] at both the transmitter and receiver. For instance, Coordinate-Interleaving (CI) was combined with IM in [28] for the sake of achieving further diversity gains, where the real and imaginary parts of each consecutive pair of PSK/QAM symbols were swapped. Furthermore, sophisticated Compressed Sensing (CS) techniques were conceived in the literature for several functions, such as symbol detection [29], sparse channel estimation [30] and more lately for information precoding [31]. To expound a little further, CS-assisted precoding used in IM-aided transceivers is

capable of enhancing their spectral efficiency by compressing the high-dimensional transmitted IM block of the *virtual domain* into a low-dimensional block in the classic *frequency domain*, which can reduce the size of the transmitted symbol without reducing the amount of transmitted information [31].

Additionally, to employ a powerful coding scheme, which is essential for achieving an infinitesimally low Bit Error Rate (BER) at near-capacity SNRs, soft-decision (SD)-aided detection, rather than the classical Hard-Decision (HD)-aided detection is required at the receiver [32]. Iterative decoding techniques associated with SD bit weighing allow us to invoke the powerful tool of EXtrinsic Information Transfer chart [33] for evaluating the convergence behavior of SD-aided coded systems.

Against this background, in this paper, we propose a holistic physical-layer transceiver design, which hinges on the concepts of OFDM-IM and STSK as the core information bearer. Then we amalgamate it with coordinate interleaving and CS for achieving further enhanced diversity gains and spectral efficiency. Furthermore, we intrinsically amalgamate it with ABF to mitigate the effect of the path loss imposed by the mmWave channel. To elaborate a little further, our contributions in this treatise can be summarized as follows:

- We conceive a CS-aided STSK-IM scheme for mmWave communications, which is an amalgam of OFDM-IM, STSK, CS, CI and hybrid beamforming. Furthermore, we present both the HD-aided and SD-aided detectors combined with a two-stage serially concatenated design. Then, we introduce our low-complexity detector, which operates on a block-by-block basis.
- We employ CS precoding at the transmitter side for compressing sparse OFDM-IM blocks prior to transmission, which enhances the system's spectral efficiency and improves its BER performance.
- Furthermore, we present a pair of Frequency Index (FI) mapping techniques, namely the Distinct FI (DFI) and the Shared FI (SFI) arrangements, which determine the grade of sparsity of the OFDM symbol as well as the achievable capacity.
- We formulate the Discrete-Input Continuous-Output Memoryless Channel (DCMC) capacity of the system presented.
- We invoke the powerful tool of EXIT charts for evaluating the capacity of the SD-aided system associated with our reduced-complexity detector.

The remainder of the paper is organized as follows. In Section II, we introduce our CS-aided STSK-IM system model, which includes both the transmitter and receiver architecture, as well as our the optimal and sub-optimal detection techniques, followed by the proposed allocation schemes in addition to the beamforming scheme employed. Next, the DCMC capacity analysis is presented in Section III. Section IV provides our numerical results, while our conclusions are offered in Section V.

II. System Model

Consider the architecture of the CS-aided STSK-IM transceiver depicted in Figure 1. In the CS-aided STSK-IM scheme, information is encoded into OFDM symbols having a large number $\bar{N}_{sc}$ of sub-carriers, which are divided into G OFDM blocks, where each OFDM block occupies $N_a = \bar{N}_{sc}/G$ sub-carriers of the whole OFDM symbol. Furthermore, information is carried both by activating K out of N_a sub-carriers in each OFDM block to implicitly transmit their indices, while keeping the remaining sub-carriers inactive and by generating K STSK codewords, which are consolidated into the activated K sub-carriers. We choose STSK as the core codeword by virtue of its immense advantages in terms of striking a compelling diversity versus multiplexing gain trade-off in a MIMO system.

However, owing to the fact that the transmitted information is not mapped to all sub-carriers, and hence less information is transmitted per block, we compensate for the resultant throughput loss by introducing the concept of CS precoding. More specifically, in the CS-aided STSK-IM scheme we compress the N_a-sub-carrier OFDM block, which is termed as the virtual domain in Figure 1, into a smaller block of $N_f \leq N_a$ sub-carriers, which we refer to as the classic frequency domain in Figure 1, and hence a total of $\bar{N}_{sc}$ virtual sub-carriers are compressed and transmitted over N_{sc} frequency sub-carriers, given that $N_{sc} \gg \bar{N}_{sc}$. More explicitly, we exploit the capability of CS to compress the information in N_a-sub-carrier OFDM blocks of the virtual domain into smaller OFDM blocks of the classic frequency domain of the sub-carriers. In

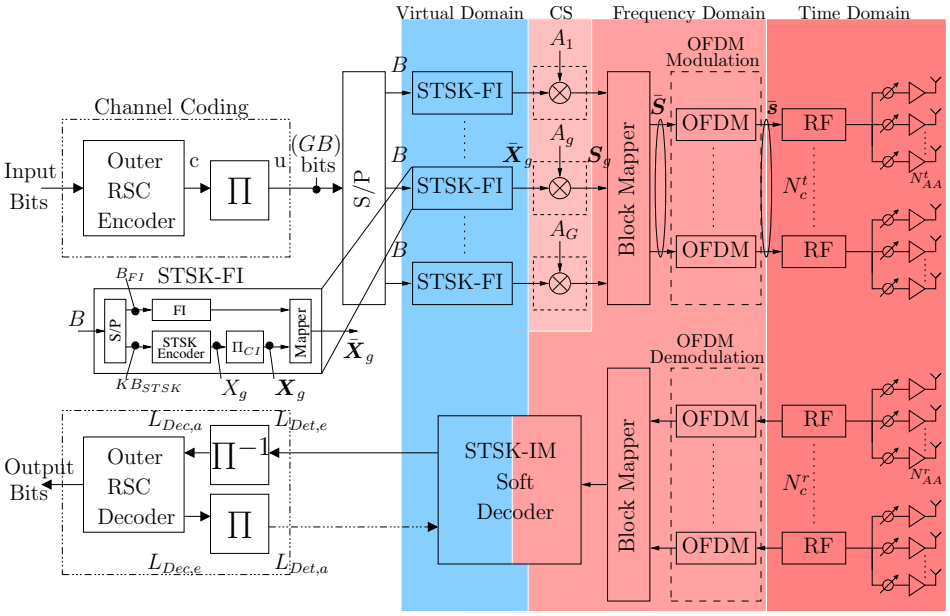

Figure 1. Block diagram of the CS-aided STSK-IM transceiver.

what follows, we introduce our CS-aided STSK-IM scheme.

A. Transmitter

In the CS-aided STSK-IM transmitter of Figure 1, which is equipped with $N_c^t = M$ AAs[1], a total of $(G \cdot B)$ bits are fed into the STSK-IM system following channel encoding part transmitting a total of G OFDM blocks. These $(G \cdot B)$ bits are then divided into G groups each having B bits, which are then fed into G STSK-FI encoders. The detailed STSK-IM encoding process is further illustrated in Figure 2. Each of the encoders generates an OFDM block of N_a sub-carriers, where the G blocks generated constitute the whole $(N_a \cdot G)$-element virtual OFDM symbol in the virtual domain[2] of Figure 1. Additionally, the structure of the STSK-FI encoder is further characterized in Figure 1. To elaborate further, the B-bit input sequence of the g-th STSK-FI encoder is further split into $(K \cdot B_{STSK})$ bits and the B_{FI} bits with the aid of the S/P portrayed in Figure 1, where we have $g = 1, \ldots, G$. The first $(K \cdot B_{STSK})$ bits are fed into the STSK encoder in order to generate K STSK codewords $\{\mathbf{x}_k\}_{k=1}^{K}$, which are incorporated into the matrix X_g, as depicted in cyan color in Figure 2. An STSK codeword $\mathbf{x} \in \mathbb{C}^{M \times T}$ can be expressed as

$$\mathbf{x} = \boldsymbol{D}_q x_l, \tag{1}$$

where $\boldsymbol{D}_q \in \mathbb{C}^{M \times T}$ is the q-th space-time dispersion matrix, which is generated based on the random-search approach of [22] under the power constraint of $\text{trace}\left\{\boldsymbol{D}_q \boldsymbol{D}_q^H\right\} = T$ and is used for dispersing the l-th $\mathcal{L}$-PSK/QAM symbol x_l over M spatial dimensions and T time slots. The K STSK codewords are then processed using the CI-interleaver $\prod_{CI}$ shown in Figure 1 that swaps the real and the imaginary parts of every pair of consecutive codewords of the K available STSK codewords for attaining an improved diversity gain. Hence, the interleaved version of X_g can be expressed as $\boldsymbol{X}_g = \{\mathring{\mathbf{x}}_k\}_{k=1}^{K} = \{\boldsymbol{X}_{g,T_i}\}_{T_i=1}^{T}$, where $\mathring{\mathbf{x}}_k$ is the k-th interleaved STSK codeword and $\boldsymbol{X}_{g,T_i}$ is the T_i-th component of $\boldsymbol{X}_g$, as illustrated in light blue color in Figure 2. On a side note, an STSK codeword is dispersed over T STSK time slots, hence in order to utilize the classic OFDM modulation in our system, each $(M \times T)$-element STSK codeword is mapped into T OFDM symbols given that each T_i-th component of each of the generated STSK codewords is mapped onto the same OFDM symbol as per [8], [15], [23], [26], [34], given that we have $T_i = 1, \ldots, T$. For further illustration, an example is provided later in this section.

[1]An AA is a group of closely spaced AEs, which is widely used for mmWave communications for performing beamforming.

[2]The pre-CS stage is denoted as the virtual domain.

The other B_{FI} bits are utilized by the FI component of the STSK-FI encoder of Figure 1 to select a combination of K out of N_a sub-carriers in order to map the transmitted information their indices. This allows the STSK-IM system to convey information both over the K STSK codewords and in form of the implicit information of the K activated sub-carrier indices of $\bar{\boldsymbol{X}}_g$, with $\bar{\boldsymbol{X}}_g$ being the g-th 3D virtual block output of the g-th STSK-FI encoder visualized in Figure 2, which has a total of T sub-OFDM blocks $\bar{\boldsymbol{X}}_{g,T_i} \in \mathbb{C}^{N_a \times M}$. To expound a little further, the mapper of the STSK-FI encoder of Figure 1 assigns K out of N_a virtual domain sub-carriers to accommodate $\boldsymbol{X}_g$ in $\bar{\boldsymbol{X}}_g$, where $\boldsymbol{X}_{g,T_i}$ is the $(M \times K)$-element T_i-th component of $\boldsymbol{X}_g$, which is shown in magenta on $\boldsymbol{X}_g$ in Figure 2. Furthermore, the magenta segment of $\bar{\boldsymbol{X}}_g = \{\bar{\boldsymbol{X}}_{g,T_i}\}_{T_i=1}^{T}$ in Figure 2 symbolizes $\bar{\boldsymbol{X}}_{g,T_i}$ and its $(N_a \times M)$-element constituent transmitted within the G blocks at the T_i-th time slot.

After mapping the K interleaved STSK codewords to their corresponding activated sub-carriers, the intrinsic mapper of the STSK-FI encoder of Figure 1 simultaneously maps the T components of $\boldsymbol{X}_g$ to the selected sub-carriers. Hence, the T_i-th constituent $\bar{\boldsymbol{X}}_{g,T_i} \in \mathbb{C}^{N_a \times M}$ of the g-th 3D virtual block $\bar{\boldsymbol{X}}_g$ output of the STSK-FI encoder can be expressed as

$$\bar{\boldsymbol{X}}_{g,T_i} = \boldsymbol{F}_g \cdot \boldsymbol{X}_{g,T_i}, \tag{2}$$

given that $\boldsymbol{X}_{g,T_i} \in \mathbb{C}^{M \times K}$ is the T_i-th constituent of the CI-interleaved codewords $\{\mathring{\mathbf{x}}_k\}_{k=1}^{K}$, as shown in Figure 2, while $\boldsymbol{F}_g$ represents the $(N_a \times M)$-element sub-carrier activation matrix having K non-zero elements and a maximum of one non-zero component per row, which can be expressed as

$$\boldsymbol{F}_g = \begin{bmatrix} 0 & \cdots & 0 & \cdots & 1 & \cdots & 0 \\ \vdots & \ddots & \vdots & \ddots & \vdots & \ddots & \vdots \\ 0 & \cdots & 1 & \cdots & 0 & \cdots & 0 \end{bmatrix}^{T}, \tag{3}$$

where the row index in the k-th column of $\boldsymbol{F}_g$ characterizes the sub-carrier index assigned for the k-th component of the CI-interleaved STSK codeword of $\boldsymbol{X}_{g,T_i}$. To elaborate a little further, consider an STSK-IM system associated with $N_a = 4$ and $K = 2$, where the second and third sub-carriers of $\boldsymbol{X}_g$ are activated. Assuming that $M = 2$ and $T = 2$, $\boldsymbol{X}_g$ can be formulated as

$$\boldsymbol{X}_g = \left\{ \underbrace{\begin{bmatrix} \mathring{\boldsymbol{x}}_{1,1}^{(1)} & \mathring{\boldsymbol{x}}_{1,2}^{(1)} \\ \mathring{\boldsymbol{x}}_{2,1}^{(1)} & \mathring{\boldsymbol{x}}_{2,2}^{(1)} \end{bmatrix}}_{\mathring{\mathbf{x}}_1}; \underbrace{\begin{bmatrix} \mathring{\boldsymbol{x}}_{1,1}^{(2)} & \mathring{\boldsymbol{x}}_{1,2}^{(2)} \\ \mathring{\boldsymbol{x}}_{2,1}^{(2)} & \mathring{\boldsymbol{x}}_{2,2}^{(2)} \end{bmatrix}}_{\mathring{\mathbf{x}}_2} \right\}, \tag{4}$$

where $\mathring{\boldsymbol{x}}_{M_i,T_i}^{(k)}$ denotes the coefficients of $\boldsymbol{X}_g$ char-

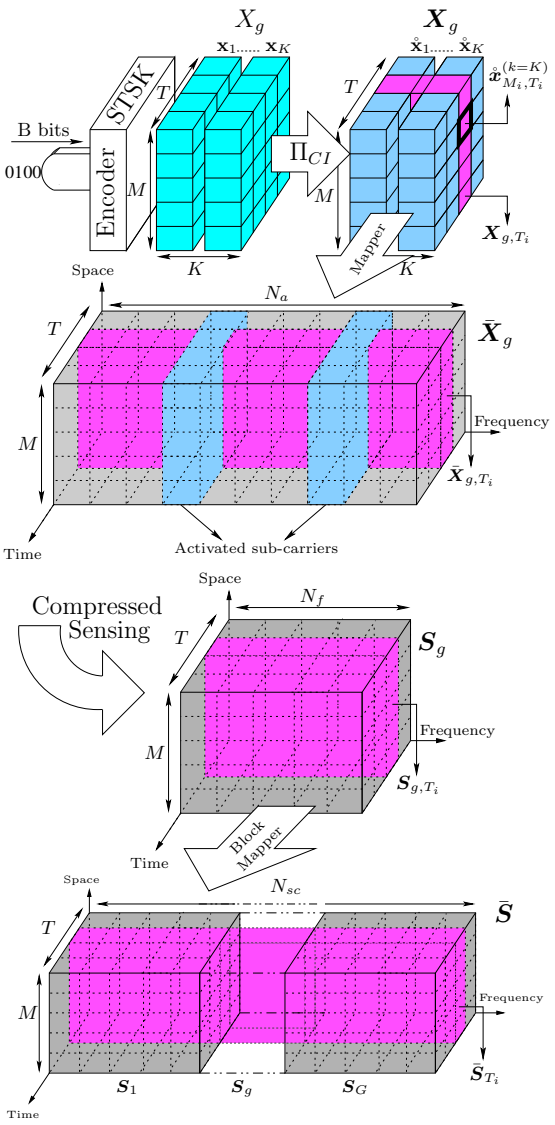

Figure 2. An illustration of the process of generating $\bar{\boldsymbol{S}}$ the frequency domain OFDM super-symbol. Starting from the B input bits to the g-th STSK-FI encoder of Figure 1, where K STSK codewords X_g are generated (in cyan) and then interleaved with the aid of $\prod_{CI}$ to get $\boldsymbol{X}_g$ the interleaved STSK codewords (in light blue). The Mapper then maps the K constituents of $\boldsymbol{X}_g$ into the virtual domain block $\bar{\boldsymbol{X}}_g$, where the K out of N_a activated FIs are shown in light blue. Next, the frequency domain block $\boldsymbol{S}_g$ is produced after applying CS and finally, the Block Mapper maps the G block $\{\boldsymbol{S}_g\}_{g=1}^{G}$ into the OFDM super-symbol $\bar{\boldsymbol{S}}$. The T_i-th segment of each part, which is transmit over the T_i-th time slot is shown in magenta.

acterizing the IC-interleaved STSK codeword[3], as shown in Figure 2 given that $M_i = 1, \ldots, M$. Furthermore, the T_i-th component of $\boldsymbol{X}_g$ constitutes the T_i-th columns of both $\mathring{\mathbf{x}}_1$ and $\mathring{\mathbf{x}}_2$ of (4) as

$$\boldsymbol{X}_{g,T_i} = \begin{bmatrix} \mathring{\boldsymbol{x}}_{1,T_i}^{(1)} & \mathring{\boldsymbol{x}}_{1,T_i}^{(2)} \\ \mathring{\boldsymbol{x}}_{2,T_i}^{(1)} & \mathring{\boldsymbol{x}}_{2,T_i}^{(2)} \end{bmatrix}. \tag{5}$$

Now, to activate for example the second and third sub-carriers of $\bar{\boldsymbol{X}}_g$, the sub-carriers activation matrix $\boldsymbol{F}_g$ can be formulated as

$$\bar{\boldsymbol{X}}_{g,T_i} = \underbrace{\begin{bmatrix} 0 & 0 \\ 1 & 0 \\ 0 & 1 \\ 0 & 0 \end{bmatrix}}_{\boldsymbol{F}_g} \cdot \underbrace{\begin{bmatrix} \mathring{\boldsymbol{x}}_{1,T_i}^{(1)} & \mathring{\boldsymbol{x}}_{1,T_i}^{(2)} \\ \mathring{\boldsymbol{x}}_{2,T_i}^{(1)} & \mathring{\boldsymbol{x}}_{2,T_i}^{(2)} \end{bmatrix}}_{\boldsymbol{X}_{g,T_i}}, \tag{6}$$

$$= \begin{bmatrix} 0 & \mathring{\boldsymbol{x}}_{1,T_i}^{(1)} & \mathring{\boldsymbol{x}}_{1,T_i}^{(2)} & 0 \\ 0 & \mathring{\boldsymbol{x}}_{2,T_i}^{(1)} & \mathring{\boldsymbol{x}}_{2,T_i}^{(2)} & 0 \end{bmatrix}^T, \tag{7}$$

which translates to

$$\bar{\boldsymbol{X}}_{g,(T_i=1)} = \begin{bmatrix} 0 & \mathring{\boldsymbol{x}}_{1,1}^{(1)} & \mathring{\boldsymbol{x}}_{1,1}^{(2)} & 0 \\ 0 & \mathring{\boldsymbol{x}}_{2,1}^{(1)} & \mathring{\boldsymbol{x}}_{2,1}^{(2)} & 0 \end{bmatrix}^T, \tag{8}$$

and

$$\bar{\boldsymbol{X}}_{g,(T_i=2)} = \begin{bmatrix} 0 & \mathring{\boldsymbol{x}}_{1,2}^{(1)} & \mathring{\boldsymbol{x}}_{1,2}^{(2)} & 0 \\ 0 & \mathring{\boldsymbol{x}}_{2,2}^{(1)} & \mathring{\boldsymbol{x}}_{2,2}^{(2)} & 0 \end{bmatrix}^T. \tag{9}$$

Observe that $\bar{\boldsymbol{X}}_{g,(T_i=1)}$ and $\bar{\boldsymbol{X}}_{g,(T_i=2)}$ in (8) and (9) resembles two OFDM blocks with $N_a = 4$ sub-carriers, which collectively construct the g-th OFDM block constituting T OFDM sub-blocks at the time slots $T_i = 1$ and $T_i = 2$, respectively, while having the second and the third sub-carriers activated.

At the output of the g-th STSK-FI encoder of Figure 1, the g-th virtual block is refined using the CS measurement matrix $\mathbf{A}_g$ that transforms it into the frequency domain and compresses its size from N_a sub-carriers into $N_f \leq N_a$ sub-carriers, where $\mathbf{A}_g$ is universal and is preassigned equivalently to all of the G blocks. More specifically, the T_i-th component of the g-th virtual block $\boldsymbol{X}_g$ can be transformed into the frequency domain upon multiplying it by $\mathbf{A}_g \in \mathbb{C}^{N_f \times N_a}$ as

$$\boldsymbol{S}_{g,T_i} = \mathbf{A}_g \cdot \bar{\boldsymbol{X}}_{g,T_i}, \tag{10}$$

$$= \left[\boldsymbol{A}_{g,1} \cdots \boldsymbol{A}_{g,n_f} \cdots \boldsymbol{A}_{g,N_f}\right]^T \cdot \bar{\boldsymbol{X}}_{g,T_i}, \tag{11}$$

where $\boldsymbol{S}_{g,T_i} \in \mathbb{C}^{N_f \times M}$ is the T_i-th component of the g-th frequency domain 3D block $\boldsymbol{S}_g = \{\boldsymbol{S}_{g,T_i}\}_{T_i=1}^{T}$, as visualized in Figure 2, with $\boldsymbol{A}_{g,n_f} \in \mathbb{C}^{1 \times N_a}$ being the n_f-th row vector of $\mathbf{A}_g$. The CS measurement matrix $\mathbf{A}_g$ is generated based on the constraint of having its mutual coherence lower than $1/(2K-1)$, which ensures that the column vectors of $\mathbf{A}_g$ are as uncorrelated as possible in order to achieve efficient recovery at the receiver as per [27], [35].

After obtaining all of the G frequency domain OFDM blocks $\{\boldsymbol{S}_g\}_{g=1}^{G}$ constituting N_f sub-carriers, the block mapper of Figure 1 then maps all blocks into a single OFDM super symbol $\bar{\boldsymbol{S}} = \{\bar{\boldsymbol{S}}_{T_i}\}_{T_i=1}^{T}$ comprising T OFDM symbols of $(G \cdot N_f \times M) = (N_{sc} \times M)$ elements. To visualize $\bar{\boldsymbol{S}}$, imagine G multiples of the frequency domain blocks $\boldsymbol{S}_g$ aligned horizontally, as illustrated in Figure 2, where the collective aggregate of their magenta colored sub-block $\boldsymbol{S}_{g,T_i}$ characterizes the T_i-th OFDM symbol $\bar{\boldsymbol{S}}_{T_i} \in \mathbb{C}^{N_{sc} \times M}$.

Next, inverse FFT (IFFT) is applied to each sub-OFDM symbol, which is the m-th row of the magenta segment of $\boldsymbol{S}_g$ depicted in Figure 2 in order to get the time domain super-symbol $\bar{\boldsymbol{s}}$ seen in Figure 1 followed by concatenating an N_{cp}-long CP at its head for the sake of overcoming the ISI imposed by the mmWave multipath channel. Finally, ABF is applied in the analogue domain with the aid of $N_t = (N_c^t \cdot N_{AA}^t)$ phase-shifters applied at the head of each AE.

B. Receiver

The CS-aided STSK-IM receiver of Figure 1 is equipped with N_c^r receive AAs, which is equivalent to the number of the receive RF chains, where each AA is connected to N_{AA}^r receive AEs on their front ends. The complex-valued wireless channel envelope is assumed to be constant over the transmission duration of the OFDM super-symbol $\bar{\boldsymbol{s}}$ as well as the CP.

Upon receiving the OFDM super-symbol, ABF is applied to the received signal with the aid of the $(N_c^r \times N_{AA}^r)$ phase-shifters. The beamformed signal

[3] $\mathring{\boldsymbol{x}}_{M_i,T_i}^{(k)}$ is the interleaved version of $\boldsymbol{x}_{M_i,T_i}^{(k)}$ denoting the coefficients of X_g.

is then fed into the OFDM demodulators of Figure 1, which removes the CP attached and FFT-based detection is invoked. The equivalent frequency domain signal $Y_{T_i}(n_{sc}) \in \mathbb{C}^{N_c^r \times T}$ received at the n_{sc}-th sub-carrier during the T_i-th time slot can be expressed as

$$\begin{aligned} Y_{T_i}(n_{sc}) &= W_{RF}^r(n_{sc}) \cdot H(n_{sc}) \cdot W_{RF}^t(n_{sc}) \cdot \bar{\boldsymbol{S}}_{T_i}(n_{sc}) \\ &\quad + \bar{V}_{T_i}(n_{sc}), \qquad (12) \\ &= \boldsymbol{H}(n_{sc}) \cdot \bar{\boldsymbol{S}}_{T_i}(n_{sc}) + \bar{V}_{T_i}(n_{sc}), \qquad (13) \end{aligned}$$

where $\bar{\boldsymbol{S}}_{T_i}(n_{sc}) \in \mathbb{C}^{N_c^t \times 1}$ denotes the n_{sc}-th column of $\bar{\boldsymbol{S}}_{T_i}$ depicted in Figure 2 given that $M = N_c^t$, $W_{RF}^r(n_{sc}) \in \mathbb{C}^{N_c^r \times N_r}$ is the equivalent receive ABF weight matrix, $H(n_{sc}) \in \mathbb{C}^{N_r \times N_t}$ is the frequency domain channel matrix at the n_{sc}-th sub-carrier and $W_{RF}^t(n_{sc}) \in \mathbb{C}^{N_t \times N_c^t}$ is the equivalent transmit ABF weight matrix. $\bar{V}(n_{sc}) \in \mathbb{C}^{N_c^r \times T}$ is the frequency domain noise vector after applying the receive ABF as $\bar{V}_{T_i}(n_{sc}) = W_{RF}^r(n_{sc}) \cdot V_{T_i}(n_{sc})$, given that $V_{T_i}(n_{sc}) \in \mathbb{C}^{N_r \times T}$ is the Additive White Gaussian Noise (AWGN) satisfying $\mathcal{CN}(0, 1)$. Additionally, $\boldsymbol{H}(n_{sc}) = W_{RF}^r(n_{sc}) \cdot H(n_{sc}) \cdot W_{RF}^t(n_{sc})$ represents the $(N_c^r \times N_c^t)$-element effective digital channel matrix after applying both transmit ABF and receive ABF as well as FFT. The joint transmit-receive ABF technique employed is detailed in the following section.

Since the information transmitted in each block is dispersed over N_a sub-carriers, T time slots and M spatial dimensions, we extend the received signal model per sub-carrier seen in (12) to represent the whole block as

$$\begin{aligned} \mathbf{Y}_g &= \mathbf{H}_g \cdot \mathbf{S}_g + \mathbf{V}_g, \qquad (14) \\ &= \mathbf{H}_g \cdot \mathbf{A} \cdot \bar{\mathbf{X}}_g + \mathbf{V}_g, \qquad (15) \\ &= \mathbf{H}_g \cdot \mathbf{A} \cdot \mathbf{F}_g \cdot \mathbf{X}_g + \mathbf{V}_g, \qquad (16) \end{aligned}$$

given that $\mathbf{Y}_g \in \mathbb{C}^{N_f N_c^r \times T}$ is the g-th received block, $\mathbf{H}_g \in \mathbb{C}^{\left(N_f N_c^r\right) \times \left(N_f N_c^t\right)}$ denotes the block-equivalent representation of the N_f channel matrices in the g-th block, $\mathbf{A} \in \mathbb{C}^{\left(N_f M\right) \times (N_a M)}$ denotes the block-equivalent CS matrix of $\mathbf{A}_g$, $\mathbf{F}_g \in \mathbb{C}^{(N_a M) \times (KM)}$ is the block-equivalent representation of the FI mapping $\boldsymbol{F}_g$ of (3). Furthermore, $\mathbf{X}_g \in \mathbb{C}^{(KM) \times T}$ in Equation (16) indicates the block-equivalent matrix containing the K interleaved STSK codeword of $\boldsymbol{X}_g$ of Equation (2), while $\bar{\mathbf{X}}_g \in \mathbb{C}^{(N_a M) \times T}$ denotes the g-th virtual domain block. The equivalent system model of (14) can be further expressed as

$$\begin{bmatrix} \mathbf{Y}_{g,1} \\ \vdots \\ \mathbf{Y}_{g,n_f} \\ \vdots \\ \mathbf{Y}_{g,N_f} \end{bmatrix} = \begin{bmatrix} \mathbf{H}_{g,1} & \mathbf{0} & \cdots & \cdots & \mathbf{0} \\ \mathbf{0} & \ddots & \mathbf{0} & \cdots & \vdots \\ \vdots & \ddots & \mathbf{H}_{g,n_f} & \ddots & \vdots \\ \vdots & \cdots & \mathbf{0} & \ddots & \mathbf{0} \\ \mathbf{0} & \cdots & \cdots & \mathbf{0} & \mathbf{H}_{g,N_f} \end{bmatrix} \cdot \begin{bmatrix} \mathbf{A}_1 \\ \vdots \\ \mathbf{A}_{n_f} \\ \vdots \\ \mathbf{A}_{N_f} \end{bmatrix} \cdot \mathbf{F}_g \cdot \mathbf{X}_g + \mathbf{V}_g, \qquad (17)$$

where $\mathbf{Y}_{g,n_f} \in \mathbb{C}^{N_c^r \times T}$ represents the signal received at the n_f-th sub-carrier of group g, $\mathbf{H}_{g,n_f} \in \mathbb{C}^{N_c^r \times N_c^t}$ is the effective channel at the n_f-th sub-carrier of group g, $\mathbf{A}_{n_f} \in \mathbb{C}^{M \times (N_a M)}$ denotes the block-diagonal equivalent representation of $\boldsymbol{A}_{g,n_f}$, while the n_f-th row vector $\mathbf{A}_g$ formulated in (11) is given by

$$\begin{aligned} \mathbf{A}_{n_f} &= \boldsymbol{I}_T \otimes \boldsymbol{A}_{g,n_f}, \qquad (18) \\ &= \begin{bmatrix} \boldsymbol{A}_{g,n_f} & \cdots & \mathbf{0} \\ \vdots & \ddots & \vdots \\ \mathbf{0} & \cdots & \boldsymbol{A}_{g,n_f} \end{bmatrix}, \qquad (19) \end{aligned}$$

with $\boldsymbol{I}_T$ being the $(T \times T)$-element identity matrix and $\otimes$ being the Kronecker product. Similarly, $\mathbf{F}_g$ can be expressed as $\mathbf{F}_g = \boldsymbol{I}_M \otimes \boldsymbol{F}_g$ given that $\boldsymbol{I}_M$ is the $(M \times M)$-element identity matrix and finally, $\mathbf{X}_g$ can be formulated as

$$\mathbf{X}_g = \begin{bmatrix} \mathring{\mathbf{x}}_1 & \cdots & \mathring{\mathbf{x}}_k & \cdots & \mathring{\mathbf{x}}_K \end{bmatrix}^T. \qquad (20)$$

We use these diagonalized and blocked representations instead of the classical matrix multiplication to integrate all the coefficients associated with the N_f classical sub-carriers, N_a virtual sub-carriers, T time slots and M spatial dimensions into a single operation.

Having presented the received space-time-frequency block $\mathbf{Y}_g$ in (16), in what follows we detail our HD-aided detection algorithms as well as their SD-aided counterparts.

C. Optimal Detection Techniques

In this section, we introduce both the ML detector and the reduced-complexity detector.

1) HD-aided Maximum Likelihood Detection: Let us assume that $\langle q_k, l_k, c\rangle$ correspond to the specific input bits of an STSK-IM block, which are mapped to both the q_k-th dispersion matrix and l_k-th PSK/QAM symbol in the $k = 1, \ldots, K$ STSK codeword $(\mathbf{X})_{q_k,l_k}$ of $\mathbf{X}$ as well as the c-th FI mapping matrix $\mathbf{F}_c$, given that the total number of FI mapping matrices is $c = 1, \ldots, N_c$. Then, the estimates of $\langle q_k, l_k, c\rangle$ given by $\left\langle \hat{q}_k, \hat{l}_k, \hat{c} \right\rangle$ are expressed as

$$\left\langle \hat{q}_k, \hat{l}_k, \hat{c} \right\rangle = \arg\min_{q_k,l_k,c} \left\| \mathbf{Y}_g - \mathbf{H}_g \cdot \bar{\mathbf{S}} \right\|, \quad (21)$$

$$= \arg\min_{q_k,l_k,c} \left\| \mathbf{Y}_g - (\mathbf{H}_g \cdot \mathbf{A}) \cdot \mathbf{F}_c \cdot (\mathbf{X})_{q_k,l_k} \right\| \quad (22)$$

$$= \arg\min_{q_k,l_k,c} \left\| \mathbf{Y}_g - (\mathbf{H}_g \cdot \mathbf{A})_c \cdot (\mathbf{X})_{q_k,l_k} \right\|, \quad (23)$$

where $\bar{\mathbf{S}}$ is the search-space of the STSK-IM system defined as $\bar{\mathbf{S}} = \left(\mathbf{A} \cdot \mathbf{F}_c \cdot (\mathbf{X})_{q_k,l_k}\right)$, while $(\mathbf{H}_g \cdot \mathbf{A})_c$ constitutes the column vectors of $(\mathbf{H}_g \cdot \mathbf{A})$ mapped to the c-th FI selection. The ML detector achieves the optimal detection performance in uncoded hard-decision scenarios.

2) Log-MAP Detection : Having presented the ML detector for the uncoded CS-aided STSK-IM system, we present our soft-decision aided iterative detection technique, as per the system depicted in Figure 1. This class of detection is essential in practical scenarios, where powerful channel coding techniques are employed, such as turbo coding [36].

The two-stage serially concatenated system of Figure 1 incorporates an amalgam of our STSK-IM detector and a half-rate Recursive Systematic Convolutional (RSC) code, which are connected by an interleaver $\prod$ and deinterleaver $\prod^{-1}$ pair. To expound a little further, the STSK-IM decoder of Figure 1 obtains the extrinsic LLR $L_{Det,e}$ using both the received signal $\mathbf{Y}_g$ and the *a priori* LLRs $L_{Det,a}$, which are gleaned by interleaving the extrinsic output $L_{Dec,e}$ of the RSC decoder using the interleaver $\prod$ of Figure 1.

Having received the signal $\mathbf{Y}_g$ of (14) that comprises $(G \cdot B)$ coded bits $\mathbf{b} = \left[b_1, b_2, \ldots, b_{(G \cdot B)}\right]$, the extrinsic LLR of $b_i \in \mathbf{b}$ given by $L_{Det,e}(b_i)$ can be obtained by the STSK-IM detector after invoking the Approx-Log-MAP algorithm as [36]

$$L_{Det,e}(b_i) = \underset{\bar{\mathbf{s}} \in \bar{\mathbf{S}}_1^{b_i}}{\text{jac}}\left(\lambda_{q_k,l_k,c}\right) - \underset{\bar{\mathbf{s}} \in \bar{\mathbf{S}}_0^{b_i}}{\text{jac}}\left(\lambda_{q_k,l_k,c}\right), \quad (24)$$

where $\bar{\mathbf{S}}_1^{b_i}$ and $\bar{\mathbf{S}}_0^{b_i}$ denote the CS-aided STSK-MI mapping bit-sets satisfying the conditions of $\bar{\mathbf{S}}_1^{b_i} \doteq \left\{\bar{\mathbf{S}}\left(q_k, l_k, c\right) \in \bar{\mathbf{S}} : b_i = 1\right\}$ and $\bar{\mathbf{S}}_0^{b_i} \doteq \left\{\bar{\mathbf{S}}\left(q_k, l_k, c\right) \in \bar{\mathbf{S}} : b_i = 0\right\}$, respectively, given that the intrinsic metric $\lambda_{q_k,l_k,c}$ of the exponents can be formulated as

$$\lambda_{q_k,l_k,c} = -\frac{\left\| \mathbf{Y}_g - \mathbf{H}_g \cdot \bar{\mathbf{S}} \right\|^2}{N_0} + \sum_{j \neq i} b_j L_{Det,a}(b_j). \quad (25)$$

The extrinsic LLR output $L_{Det,e}$ of the STSK-IM detector is then deinterleaved using the deinterleaver $\prod^{-1}$ of Figure 1 and fed into the RSC decoder in order to obtain the *a priori* LLR $L_{Dec,a}$, as shown in Figure 1. The RSC decoder calculates, again, the extrinsic LLRs $L_{Dec,e}$ using $L_{Dec,a}$, which are again interleaved and fed into the STSK-IM detector in order to obtain the improved extrinsic LLR values $L_{Det,e}$ for the next iteration.

D. Sub-optimal Reduced Complexity-aided Detection Technique

The HD-aided ML detector introduced in Section II-C achieves an optimum performance by relying on a full-search over all the possible combinations of both the K STSK codewords associated with $\{q_k\}_{k=1}^{K}$ and $\{l_k\}_{k=1}^{K}$ as well as the FI indices $\{c\}_{c=1}^{N_c}$, thereby imposing a detection complexity order per block of $\mathcal{O}\left(N_c \times (Q \cdot \mathcal{L})^K\right)$, which is significantly higher than that of a classical OFDM-aided STSK $\mathcal{O}\left[N_a \times (Q \cdot \mathcal{L})\right]$ having the same throughput. Hence, in order to minimize the search-space of the system, we split the detection operation into two sub-operations. In the first sub-operation, we detect the FI, then we use a specific number J of FI candidates[4] to perform the ML detection. Hence, naturally , only a sub-optimum performance is achieved, as detailed below.

[4]An FI candidate denotes the index of a specific sub-carrier, which can be selected out of the available N_a sub-carriers to include it in the ML detection.

We first apply the channel equalization matrix $\boldsymbol{Z}_g$ to the g-th received block $\mathbf{Y}_g$ in order to eliminate the effect of the channel over its N_a sub-carriers, where $\boldsymbol{Z}_g$ can be expressed as

$$\boldsymbol{Z}_g = \left[(\mathbf{H}_g)^H \mathbf{H}_g + \frac{1}{\gamma} \boldsymbol{I}_{N_f M} \right]^{-1} (\mathbf{H}_g)^H, \quad (26)$$

with γ being the average SNR per symbol.

Then, the equalized signal can be expressed as

$$\begin{aligned} \boldsymbol{Z}_g \mathbf{Y}_g &= (\boldsymbol{Z}_g \mathbf{H}_g) \cdot \mathbf{A} \cdot \mathbf{F}_g \cdot \mathbf{X}_g + \boldsymbol{Z}_g \cdot \mathbf{V}_g \quad (27) \\ &= \mathbf{A} \cdot \mathbf{S}_g + \boldsymbol{Z}_g \cdot \mathbf{V}_g. \quad (28) \end{aligned}$$

The equalized signal in (28) is still in the frequency domain and thereby the FI cannot be extracted unless it is converted back into the virtual domain. Hence, in order to retrieve a rough estimate of the transmitted virtual domain block $\mathbf{X}_g$, we apply the CS equalization matrix $\tilde{\mathbf{A}}$ to (28) as

$$\left(\tilde{\mathbf{A}} \boldsymbol{Z}_g \mathbf{Y}_g \right) = \tilde{\mathbf{A}} \cdot \mathbf{A} \cdot \mathbf{S}_g + \tilde{\mathbf{A}} \cdot \boldsymbol{Z}_g \cdot \mathbf{V}_g, \quad (29)$$

where the equalization matrix employed is $\tilde{\mathbf{A}} = \mathbf{A}^H$, which then leads to

$$\tilde{\mathbf{Y}}_g = \|\mathbf{A}\|^2 \cdot \mathbf{S}_g + \tilde{\mathbf{V}}_g, \quad (30)$$

given that $\tilde{\mathbf{Y}}_g = \left(\tilde{\mathbf{A}} \boldsymbol{Z}_g \mathbf{Y}_g \right) \in \mathbb{C}^{(N_a M) \times T}$.

Next, we obtain the power of each row vector of $\tilde{\mathbf{Y}}_g$ as

$$P_g = \left[\left| \tilde{\mathbf{Y}}_{g,1} \right|^2 \quad \cdots \quad \left| \tilde{\mathbf{Y}}_{g,n_a} \right|^2 \quad \cdots \quad \left| \tilde{\mathbf{Y}}_{g,N_a} \right|^2 \right]^T, \quad (31)$$

which serves as a rough estimate of the sub-carrier's activation status in the virtual domain. For instance, in a noiseless scenario the K highest coefficients of P_g represent the K activated sub-carriers of $\bar{\mathbf{X}}_g$. However, in a noisy scenario, we choose a selection of the J highest coefficients in P_g, given that $1 \leq J \leq N_a$, which are referred to as the sub-carrier candidates. On a side note, selecting the j-th sub-carrier implies that all the FI mapping matrices $\{\mathbf{F}_c\}_{c=1}^{N_c}$ having their j-th sub-carrier activated are proportionately selected.

As in the case of implementing the HD-aided detector presented in Section II-C, the ML detection is applied to the block $\tilde{\mathbf{Y}}_g$ by invoking a full-search over all the possible combinations of the K STSK codewords having $\{q_k\}_{k=1}^K$ and $\{l_k\}_{k=1}^K$ that are associated with the J selected FI indices as follows:

$$\left\langle \hat{q}_k, \hat{l}_k, \hat{c} \right\rangle = \arg \min_{q_k, l_k, \bar{c}} \left\| \tilde{\mathbf{Y}}_g - \|\mathbf{A}\|^2 \cdot \mathbf{F}_{\bar{c}} \cdot (\mathbf{X})_{q_k, l_k} \right\|, \quad (32)$$

where $\bar{c}$ denotes the index of a total of $\bar{N}_c$ FI mapping matrices encompassing the J selected candidates. Thereupon, by selecting $J = N_a$ candidates, the RC converges to the full-space ML detector presented in (21).

On the other hand, in the case of implementing the SD-aided detector presented in Section II-C, the Approx-Log-MAP algorithm is then invoked as [36]

$$L_{Det,e}(b_i) = \underset{\bar{\mathbf{s}} \in \bar{\mathbf{s}}_1^{b_i}}{\text{jac}} \left(\lambda_{q_k, l_k, \bar{c}} \right) - \underset{\bar{\mathbf{s}} \in \bar{\mathbf{s}}_0^{b_i}}{\text{jac}} \left(\lambda_{q_k, l_k, \bar{c}} \right). \quad (33)$$

The RC-aided algorithm including both the HD-aided and the SD-aided detection techniques is detailed in Algorithm 1.

Using this sub-optimum detection technique, the complexity order of the detector can be reduced from $\mathcal{O}\left(N_c \times (Q \cdot \mathcal{L})^K \right)$ for ML detection to $\mathcal{O}\left(\bar{N}_c \times (Q \cdot \mathcal{L})^K \right)$ for the reduced-complexity detector. In the following section, we present the ABF employed in our system to overcome the high path-loss inflicted by the mmWave channel.

E. Beamforming

At the transmitter side of Figure 1, each RF chain is associated with an analogue circuitry of an N_{AA}^t-sized Antenna Array (AA) at its far end, where its AE constituents are spaced at a distance of $\lambda/2$ in order to form an angular selective beam. Similarly, each of the receive RF chains of Figure 1 is connected to an N_{AA}^r-sized AA at its front end, with the same implementation considerations taken at the transmitter. Due to the short wave-length of the mmWave signals, a large number of AEs may be accommodated within a relatively compact area in each AA for achieving a high beamforming gain [4]. Furthermore, all AAs are sufficiently far apart so that they experience uncorrelated channels. This implementation allows the system to both achieve a sufficiently high beamforming gain for mitigating the high path-loss of the mmWave channel and to

Algorithm 1 The CS-aided STSK-IM reduced-complexity detection algorithm.

Step 1: Perform channel equalization on the g-th block channel $\mathbf{H}_g$ to eliminate its effect, which can be formulated as

$$\boldsymbol{Z}_g = \left[(\mathbf{H}_g)^H \mathbf{H}_g + \frac{1}{\gamma} \boldsymbol{I}_{N_f M} \right]^{-1} (\mathbf{H}_g)^H . \tag{34}$$

Hence, the received signal after equalization can be expressed as

$$\begin{aligned} \boldsymbol{Z}_g \mathbf{Y}_g &= (\boldsymbol{Z}_g \mathbf{H}_g) \cdot \mathbf{A} \cdot \mathbf{F}_g \cdot \mathbf{X}_g + \boldsymbol{Z}_g \cdot \mathbf{V}_g & (35) \\ &= \mathbf{A} \cdot \mathbf{S}_g + \boldsymbol{Z}_g \cdot \mathbf{V}_g, & (36) \end{aligned}$$

where γ is the average SNR per symbol.

Step 2: Retrieve a rough estimate of the virtual domain block $\mathbf{X}_g$ by applying the CS equalization matrix $\tilde{\mathbf{A}}$ as

$$\left(\tilde{\mathbf{A}} \boldsymbol{Z}_g \mathbf{Y}_g \right) = \tilde{\mathbf{A}} \cdot \mathbf{A} \cdot \mathbf{S}_g + \tilde{\mathbf{A}} \cdot \boldsymbol{Z}_g \cdot \mathbf{V}_g, \tag{37}$$

where the equalization matrix employed is $\tilde{\mathbf{A}} = \mathbf{A}^H$, and hence

$$\tilde{\mathbf{Y}}_g = \|\mathbf{A}\|^2 \cdot \mathbf{S}_g + \tilde{\mathbf{V}}_g, \tag{38}$$

with $\tilde{\mathbf{Y}}_g = \left(\tilde{\mathbf{A}} \boldsymbol{Z}_g \mathbf{Y}_g \right) \in \mathbb{C}^{(N_a M) \times T}$ being the rough estimate of $\mathbf{S}_g$.

Step 3: Obtain the power of each row vector denoting the virtual sub-carriers of $\tilde{\mathbf{Y}}_{g,1}$ as

$$P_g = \left[\begin{array}{cccccc} \left| \tilde{\mathbf{Y}}_{g,1} \right|^2 & \cdots & \left| \tilde{\mathbf{Y}}_{g,n_a} \right|^2 & \cdots & \left| \tilde{\mathbf{Y}}_{g,N_a} \right|^2 \end{array} \right]^T . \tag{39}$$

Step 4: Choose a selection of J sub-carriers candidates associated with the highest values in P_g , given that $1 \leq J \leq N_a$. On a side note, selecting the j-th sub-carrier implies that all the FI mapping matrices $\{\mathbf{F}_c\}_{c=1}^{N_c}$ having the j-th sub-carrier activated are proportionately selected.

Step 5:

- **Step 5a:** In case of HD-aided detection, perform ML detection on $\tilde{\mathbf{Y}}_g$ using only the FI mapping matrices $\{\mathbf{F}_c\}_{c=1}^{N_c}$ accommodating the J selected candidates of sub-carriers as

$$\left\langle \hat{q}_k, \hat{l}_k, \hat{c} \right\rangle = \arg \min_{q_k, l_k, \bar{c}} \left\| \tilde{\mathbf{Y}}_g - \|\mathbf{A}\|^2 \cdot \mathbf{F}_{\bar{c}} \cdot (\mathbf{X})_{q_k, l_k} \right\|, \tag{40}$$

  where $\bar{c}$ denotes the index of a total of $\bar{N}_c$ FI mapping matrices encompassing the J selected candidates. Consequently, selecting $J = N_a$ candidates rather provokes the ML detector presented in (21).
- **Step 5b:** In case of SD-aided detection, determine the extrinsic LLRs of the J selected candidates using the Approx-Log-MAP algorithm as

$$L_{Det,e}(b_i) = \underset{\bar{\mathbf{s}} \in \bar{\mathbf{s}}_1^{b_i}}{\text{jac}} \left(\lambda_{q_k, l_k, \bar{c}} \right) - \underset{\bar{\mathbf{s}} \in \bar{\mathbf{s}}_0^{b_i}}{\text{jac}} \left(\lambda_{q_k, l_k, \bar{c}} \right). \tag{41}$$

simultaneously attain the independent fading needed to convey our STSK-IM information.

In this context, we consider the so-called Discrete Fourier Transform (DFT) aided codebook design of [37] for analogue beamforming in our system, which is the beamforming technique favored by the LTE standard. DFT-aided beamforming is realized in the analogue domain by relying on the $(N_c^t \cdot N_{AA}^t)$ and $(N_c^r \cdot N_{AA}^r)$ analogue phase-shifters employed at the transmitter and the receiver of Figure 1, respectively, where the weight vectors are simply a selection of column vectors of a DFT matrix.

We can reformulate the effective channel $\boldsymbol{H}$ formulated in (12) as

$$\boldsymbol{H} = W_{RF}^r \cdot H \cdot W_{RF}^t, \tag{42}$$

where the actual channel between the n_c^t-th transmit AA and the n_c^r-th receive AA is characterized by $H_{n_c^r,n_c^t} \in \mathbb{C}^{N_{AA}^r \times N_{AA}^t}$ and the sub-matrix block of the RF channel H located at its (n_c^r, n_c^t)-index is given by:

$$H = \begin{bmatrix} H_{1,1} & \cdots & H_{1,N_c^t} \\ \ddots & \iddots & \\ \vdots & H_{n_c^r,n_c^t} & \vdots \\ \iddots & \ddots & \\ H_{N_c^r,1} & \cdots & H_{N_c^r,N_c^t} \end{bmatrix}. \tag{43}$$

Furthermore, both the transmit and the receive RF beamformers W_{RF}^t and W_{RF}^r are characterized by using a block-diagonal matrix representation, where the n_c^t-th component of W_{RF}^t is defined by $\boldsymbol{w}_t^{n_{ct}} = \left[w_{n_c^t,1}^t \ \ldots \ w_{n_c^t,N_{AA}^t}^t \right]^T \in \mathbb{C}^{N_{AA}^t \times 1}$, while the n_c^r-th component of W_{RF}^r is defined as $\boldsymbol{w}_r^{n_c^r} = \left[w_{n_c^r,1}^r \ \ldots \ w_{n_c^r,N_{AA}^r}^r \right]^T \in \mathbb{C}^{1 \times N_{AA}^t}$.

Now, given that our CS-aided STSK-IM design falls under the sub-array category of MIMO systems, the transmit ABF weights of the n_c^t-th transmit AA are found by retrieving the maximum argument of the column-by-column dot product between the $(N_{AA}^t \times N_{AA}^t)$-element DFT matrix $\boldsymbol{D}_{N_{AA}^t}^t$ and the right singular matrix $\boldsymbol{V}_{n_c^t}^t \in \mathbb{C}^{N_{AA}^t \times N_{AA}^t}$ of $H_{1:N_r,n_c^t} = \boldsymbol{U}_{n_c^t}^t \boldsymbol{\Sigma}_{n_c^t}^t \boldsymbol{V}_{n_c^t}^t \in \mathbb{C}^{N_r \times N_{AA}^t}$ denoting the n_c^t-th column block of H, which can be expressed as

$$\boldsymbol{w}_t^{n_c^t} = \max \left\langle D_{n_{AA}^t}^t, \boldsymbol{V}_{n_c^t,1}^t \right\rangle_{n_{AA}^t=1}^{N_{AA}^t}, \tag{44}$$

where $D_{n_{AA}^t}^t$ denotes the n_{AA}^t-th column vector of $\boldsymbol{D}_{N_{AA}^t}^t$, $\boldsymbol{V}_{n_c^t,1}^t$ is the first singular vector of $\boldsymbol{V}_{n_c^t}^t$ and $\langle x, y \rangle$ represents the dot product of vector x and vector y. Similarly, the receive ABF weights of the n_c^r-th receive AA are determined by applying the same operation to the $(N_{AA}^r \times N_{AA}^r)$-element DFT matrix $\boldsymbol{D}_{N_{AA}^r}^t$ and to the left singular matrix $\boldsymbol{U}_{n_c^r}^r \in \mathbb{C}^{N_{AA}^r \times N_{AA}^r}$ of $H_{n_c^r,1:N_t} = \boldsymbol{U}_{n_c^r}^r \boldsymbol{\Sigma}_{n_c^r}^r \boldsymbol{V}_{n_c^t}^r \in \mathbb{C}^{N_{AA}^r \times N_t}$ denoting the n_c^r-th row block of H, which can be expressed as

$$\boldsymbol{w}_r^{n_c^r} = \max \left\langle D_{n_{AA}^r}^r, \boldsymbol{U}_{n_c^r,1}^r \right\rangle_{n_{AA}^r=1}^{N_{AA}^r}, \tag{45}$$

where $D_{n_{AA}^r}^r$ denotes the n_{AA}^r-th row vector of $\boldsymbol{D}_{N_{AA}^r}^r$ and $\boldsymbol{U}_{n_c^r,1}^r$ the first singular vector of $\boldsymbol{U}_{n_c^t}^t$. Hence, the transmit and receive phase-shifters installed at the transmit and receive AAs are oriented in the directions determined by the weights $\left\{ \boldsymbol{w}_t^{n_c^t} \right\}_{n_c^t=1}^{N_c^t}$ and $\left\{ \boldsymbol{w}_r^{n_c^r} \right\}_{n_c^r=1}^{N_c^r}$, respectively. In the following section, we will introduce a pair of FI allocation techniques, namely the SFI and DFI techniques.

F. FI Allocation Techniques

In this section, we propose two FI allocation techniques, namely the Shared Frequency Indexing (SFI) and the Distinct Frequency Indexing (DFI). More specifically, the total number of available FIs in a system associated with the SFI technique is then given by the K number of combinations out of the N_a virtual domain sub-carriers, which can be expressed as

$$N_c^{(SFI)} = \left\lfloor \binom{N_a}{K} \right\rfloor_{2^\iota}, \tag{46}$$

where $\lfloor . \rfloor_{2^\iota}$ is the flooring operation to the nearest smallest 2^ι integer operation and $\iota \geq 0$ is a positive integer.

By contrast, the total number of available FIs in a system associated with the DFI technique is then given by the total number K of distinct combinations in the N_a virtual domain sub-carriers, which can be expressed as

$$N_c^{(DFI)} = \left\lfloor \frac{N_a}{K} \right\rfloor_{2^\iota}, \tag{47}$$

where $N_c^{(DFI)}$ is considered as a special case of $N_c^{(SFI)}$ in which only the distinct combinations are

selected. Hence, B_{FI} denoting the number of the input bits entered into the FI component in the STSK-FI encoder of Figure 1 is given by $B_{FI} = \log_2(N_c)$. Hence, the total number of bits B fed into the STSK-FI encoder can be expressed as

$$B = K \cdot B_{STSK} + B_{FI}, \quad (48)$$
$$= K \cdot \log_2(\mathcal{L} \cdot Q) + \log_2(N_c). \quad (49)$$

Observe by referring to Equations (46) and (47), that a higher number of bits B_{FI} is obtained by using SFI than that with DFI. However, the DFI is capable of boosting the sparsity of the information per block, which is beneficial in terms of reducing the detection complexity, especially in systems employing CS-aided algorithms for signals estimation [27], [38].

To expound a little further on the pros and cons of both techniques, consider an STSK-IM system, where we aim for conveying for example $B_{FI} = 2$ FI bits using a total of $K = 2$ activated sub-carriers. Assuming that the SFI allocation technique is employed, we would require a minimum of $N_a = 4$ sub-carriers to attain $N_c = 4$ FI combinations, as suggested by Equation (46), yielding $B_{FI} = \log_2(4) = 2$ bits. The activated combinations are formed of K shared sub-carriers, which can for instance include the $\{1, 2\}$, $\{1, 3\}$, $\{1, 4\}$ or $\{3, 4\}$ sub-carriers, as shown in red color in Figure 3. However, by employing the DFI allocation technique, we would require $N_a = 8$ sub-carriers (the whole block in Figure 3) to attain $N_c = 4$ FI combinations based on Equation (47). The activated combinations include the $\{1, 2\}$, $\{3, 4\}$, $\{5, 6\}$ or $\{7, 8\}$ sub-carriers, as depicted in blue color in Figure 3.

To elaborate a little further on the complexity of both FI allocation techniques, in Figure 4 and Figure 5, we portray the associated complexity order denoting the search-space versus the number of selected sub-carrier candidates $J = 1, \ldots, N_a$ of an SFI-aided and a DFI-aided STSK-IM system, respectively, both associated with an STSK(2, 2, 1, BPSK) encoder as well as with $K = 2$ out of $N_a = 16$ active sub-carriers. More specifically, as the number of candidates J increases in the SFI-aided scheme depicted in Figure 4, the number $\bar{N}_c$ of FI combinations encompassing the selected sub-carriers increases quite dramatically due to having shared sub-carriers amongst the FI combination

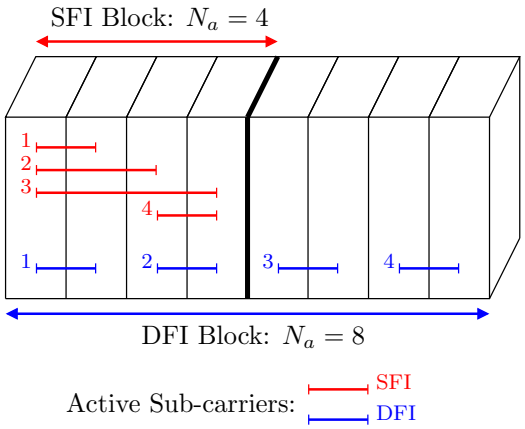

Figure 3. SFI and DFI sub-carrier allocation techniques, where the numbers represent the FI combination number.

database. Hence the search-space accommodating those FI combinations increases. For example, upon increasing the number of candidates from $J = 1$ to $J = 2$, the search-space increases on average from 41.76 to 78.58 out of the full-search space of 256, which means that only 41.76 and 78.58 out of the 256 possible of arrangements of $\bar{\mathbf{X}}_g$ are included in the search, given $J = 1$ and $J = 2$, respectively.

In a DFI-aided system, in which a single candidate associated with $J = 1$ in a $K = 2$ configuration leads to the selection of $\bar{N}_c = 1$ out of the available $N_c = 8$ FI combinations, the search-space is limited to those arrangements of $\bar{\mathbf{X}}_g$ that include the selected FI combination, which is equal to four. Hence, the system would require more candidates to attain the ML search-space of 32. This can be observed in Figure 5, where the search-space of the detector increases by four as the number of candidates is increased, which denotes the number of arrangements of $\bar{\mathbf{X}}_g$- corresponding to four - that incorporate the additional FI combination.

III. Capacity Analysis

In this section, we formulate the DCMC capacity [39] of our CS-aided STSK-IM scheme. We then invoke the powerful tool of EXIT charts to analyze the capacity of the RC-aided systems proposed in Section II-C.

A. DCMC Capacity

The DCMC capacity of our CS-aided STSK-IM system is first developed per block in order to include both the K activated codewords as well as

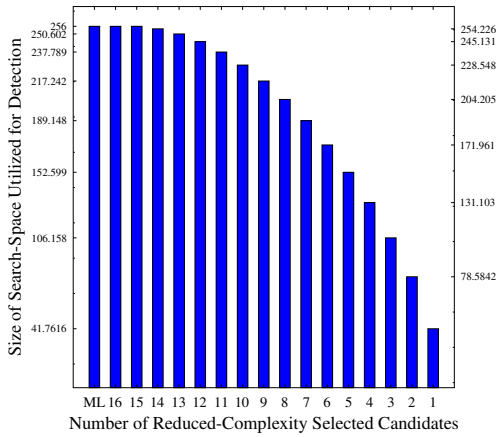

Figure 4. The search-space versus the number of selected sub-carriers candidates $J = 1, \ldots, N_a$ of a SFI-aided STSK-IM system associated with $K = 2$ out of $N_a = 16$ active sub-carriers.

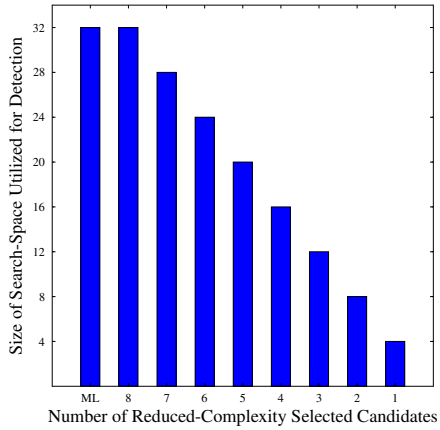

Figure 5. The search-space versus the number of selected sub-carriers candidates $J = 1, \ldots, N_a$ of a DFI-aided STSK-IM system associated with $K = 2$ out of $N_a = 16$ active sub-carriers.

the implicit FI of each block and then it is divided by the number of frequency domain sub-carriers in order to determine the capacity per sub-carrier. The DCMC capacity of our CS-aided STSK-IM scheme using $\mathcal{L}$-PSK/QAM signaling can be formulated as [39]

$$C = \frac{1}{(N_f \cdot T)} \times \max_{\left\{p\left(\overline{\mathbf{X}}\right)\right\}_{\forall q_k, l_k, c}} \sum \int_{-\infty}^{+\infty} \cdots \int_{-\infty}^{+\infty} p\left(\mathbf{Y}_g | \overline{\mathbf{X}}\right) p\left(\overline{\mathbf{X}}\right) \cdot \left[\frac{p\left(\mathbf{Y}_g | \overline{\mathbf{X}}\right)}{\sum_{\forall \overline{\mathbf{X}} \in \mathcal{X}} p\left(\mathbf{Y}_g | \overline{\mathbf{X}}'\right) p\left(\overline{\mathbf{X}}'\right)} \right] d\mathbf{Y}_g, \quad (50)$$

which is maximized when the transmitted $\mathcal{L}$-PSK/QAM symbols $p\left(\overline{\mathbf{X}}\right)$ are equiprobable, given that $p\left(\mathbf{Y}_g | \overline{\mathbf{X}}\right)$ is the conditional probability of receiving $\mathbf{Y}_g$ such that $\overline{\mathbf{X}} = (\mathbf{X})_{q_k, l_k}$ is transmitted.

Now, based on the conditional probability given by $p\left(\mathbf{Y}_g | \overline{\mathbf{X}}\right)$, the DCMC capacity can be further simplified to

$$C = \frac{1}{T} \left((G \cdot B) - \frac{1}{\left(2^{(G \cdot B)}\right)} \times \sum_{q_k, l_k, c} E \left[\log_2 \left\{ \sum_{q'_k, l'_k, c'} \exp\left(\overline{\psi}\right) \left| \overline{\mathbf{X}} \right. \right\} \right] \right), \quad (51)$$

where the intrinsic metric of the exponent $\overline{\psi}$ denoting the difference between two symbols may be expressed as

$$\overline{\psi} = -\left\| \left(\mathbf{H}_g \mathbf{A}\right) \mathbf{F}_c \left(\overline{\mathbf{X}} - \overline{\mathbf{X}}' \right) + \bar{\boldsymbol{V}} \right\|^2 + \left\| \bar{\boldsymbol{V}} \right\|^2, \quad (52)$$

with $\overline{\mathbf{X}}'$ being the transmitted symbol $\left[(\mathbf{X})_{q'_k, l'_k} \right]$.

The maximum number of bits transmitted over the N_{sc} sub-carriers can be expressed as

$$R = C \times N_{sc}. \quad (53)$$

The DCMC capacity curves of several CS-aided STSK-IM systems associated with different design specifications are depicted in Figure 6. To be specific, the DCMC capacity curves of STSK-IM systems relying on the CS characteristics of $N_f = 4$ and 8, $N_a = 8$ and 16 as well as $K = 1$, 2, 3 and 4, which are associated with the STSK(2, 2, 1, BPSK) and the STSK(2, 2, 2, BPSK) encoders using both the SFI and DFI allocation techniques are shown in Figure 6. Furthermore, we included in Figure 6 several STSK-IM systems using no CS, where no CS matrix is applied under the constraint of $N_f = N_a$ and hence, we disregard the concept of virtual to frequency domain convergence[5]. Observe in Figure 6 that the capacity curves tend towards their maximum attainable normalized throughput as the SNR value increases. Furthermore, the capacity of our system tends to increase as the number K of activated sub-carriers increases as well as the number N_c of combinations increases. To determine the

[5]We included the capacity plots of the STSK-IM system using no CS for showing the impact of employing CS on its achievable capacity limit.

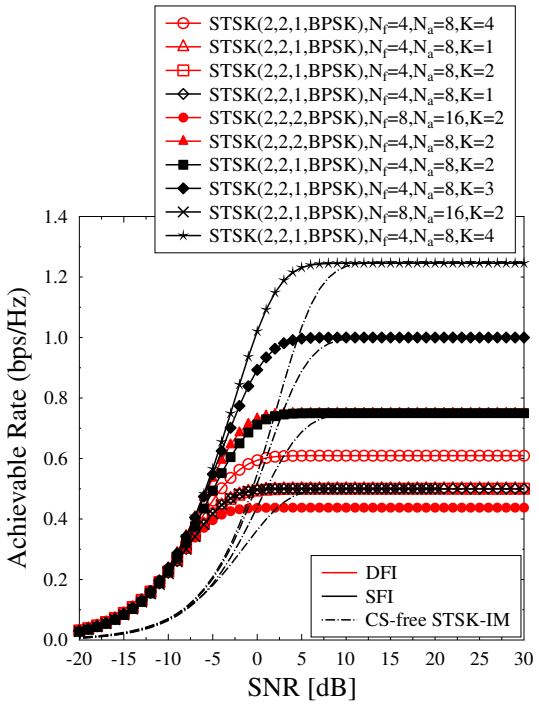

Figure 6. DCMC capacity of several CS-aided STSK-IM systems associated with the DFI and SFI allocation techniques compared to their equivalent throughput CS-free STSK-IM counterparts.

total number of bits conveyed per frequency-domain block, the normalized achievable throughput of each curve should be multiplied by its corresponding N_f value. It is also shown in Figure 6 that our CS-aided STSK-IM system is capable of achieving a higher capacity than without CS.

B. Maximum Achievable Rate Using The EXIT Chart Tool

The DCMC capacity limit formulated in (51) is closely approached by the optimum ML detector presented in Section II-C. However, by introducing the RC-aided detection technique of Section II-C, the search-space is no longer equivalent to the full-search space used for (50). Hence, we rather exploit the EXIT chart tool for analyzing the achievable capacity of the system [33]. The specific system parameters employed in this section are summarized in Table I.

In Figures 7 and 8, we portray the maximum achievable limits of a pair of RC-aided STSK-IM systems, both of which are associated with an STSK(2, 2, 1, BPSK) encoder, K =2, N_a =16 and N_f =8, where the first one relies on the DFI technique and J =1,...,8 candidates, while the other relies on the SFI technique and J =1,...,16 candidates. Observe in both figures that as the number of candidates increases, the capacity of

Parameter		Value
N_a		16
N_f		8
K		2
J	SFI	$1,\ldots,16$
	DFI	$1,\ldots,8$
Channel		mmWave
STSK(2, 2, 1, BPSK)		

Table I
SPECIFIC SYSTEM PARAMETERS OF THE STSK-IM SYSTEMS USED.

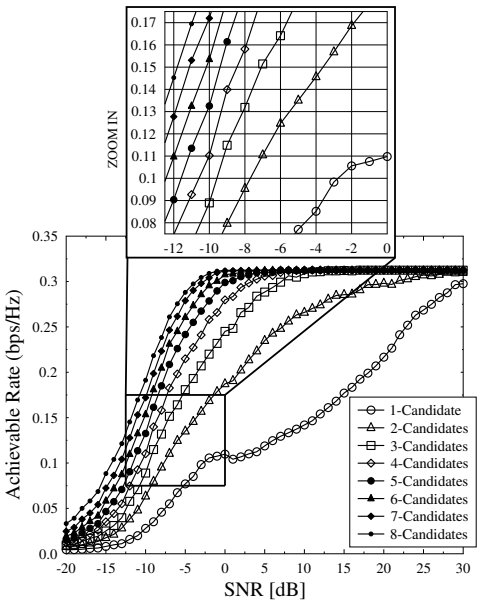

Figure 7. Maximum achievable limit of an RC-aided STSK-IM system associated with an STSK(2, 2, 1, BPSK) encoder, K =2, N_a =16 and N_f =8, which relies on the the DFI technique with J =1,...,8.

the RC-aided systems shift towards the maximum achievable capacities of their ML-aided counterparts. More specifically, observe in Figure 7 that by exploiting a single candidate in the STSK-IM system relying on the DFI technique the curve shifts further away from that maximum achievable limit, when compared to that of the SFI technique seen in Figure 8. This is due to the fact that a single candidate is used only once in DFI, while it is shared amongst several arrangements in SFI. Furthermore, observe in Figure 8 that by increasing the number of candidates to J =6, the capacity curve of the system shifts towards the maximum achievable capacity curve, despite reducing the search-space size from 256 to 171.961, as shown in Figure 4. Similar trends are also valid for the DFI-aided STSK-IM system.

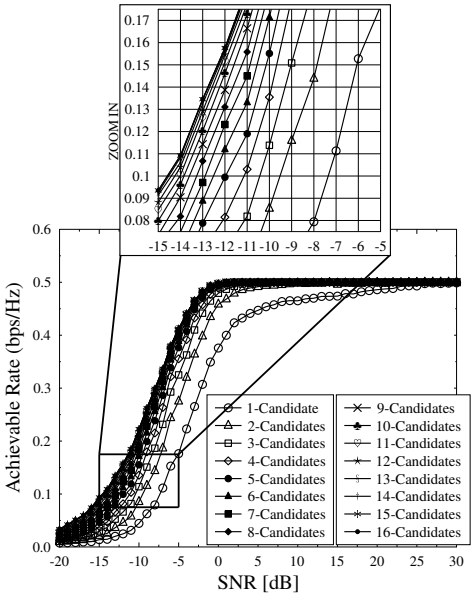

Figure 8. Maximum achievable limit of an RC-aided STSK-IM system associated with an STSK(2, 2, 1, BPSK) encoder, K =2, N_a =16 and N_f =8, which relies on the the SFI technique with J =1,. . . ,16.

Parameter		Value
N_a		16
N_f		8
K		2
J	SFI	$1, \ldots, 16$
	DFI	$1, \ldots, 8$
Channel		mmWave
Channel Coding		Uncoded RSC 1/2-rate
STSK(2, 2, 1, BPSK)		

Table II
SPECIFIC SYSTEM PARAMETERS OF THE STSK-IM SYSTEMS USED.

IV. PERFORMANCE RESULTS

In this section, we characterize the performance of our proposed CS-aided STSK-IM system for transmission over the mmWave channel, which is evaluated using Monte-Carlo simulations under the assumption of perfect CSI knowledge at both the transmitter and receiver. The specific system parameters employed in this section are summarized in Table II.

In Figures 9 and 10, we firstly portray the BER performance of our 1/2-rate RSC coded CS-aided STSK-IM system associated with SFI and DFI, respectively, where both employ an STSK(2, 2, 1, BPSK) encoder as well as N_f =8, N_a =16 and K =2 configurations upon increasing the number of iterations up to I =6. Furthermore, the SFI-aided system achieves a throughput of 8 bits per virtual block (bpvb) $\bar{\boldsymbol{X}}_g$, while the DFI-aided scheme exhibits a transmission rate of 5 bpvb. It is also shown in Figure 9 that the CS-aided STSK-IM is capable of significantly outperforming its counterpart using no CS.

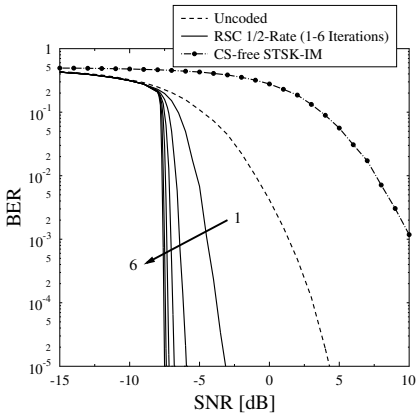

Figure 9. Achievable BER performance of our 1/2-rate RSC coded CS-aided STSK-IM system associated with an STSK(2, 2, 1, BPSK) encoder as well as N_f =8, N_a =16 and K =2 configurations associated with the SFI technique. Here, the scheme exhibited a transmission rate of 8 bits per the virtual block $\bar{\boldsymbol{X}}_g$, while employing the Approx-Log-MAP detection technique. The CS-free equivalent STSK-IM system, where N_f =N_a =16 is included as a bench mark.

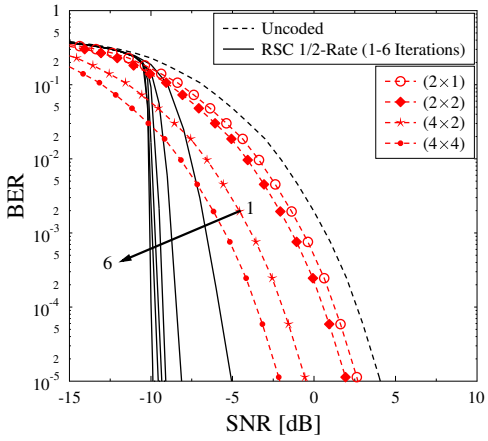

Figure 10. Achievable BER performance of our 1/2-rate RSC coded CS-aided STSK-IM system associated with an STSK(2, 2, 1, BPSK) encoder as well as N_f =8, N_a =16 and K =2 configurations associated with the DFI technique. Here, the scheme exhibited a transmission rate of 5 bits per the virtual block $\bar{\boldsymbol{X}}_g$, while employing the Approx-Log-MAP detection technique.The red curves characterize the BER performance of the system associated with $\left(N_{AA}^t \times N_{AA}^r\right)$ AAs.

Furthermore, the BER performance of the system associated with $\left(N_{AA}^t \times N_{AA}^r\right)$ arrangements is also characterized in Figure 10, in order to quantify the SNR gain of the AAs. The figure shows an SNR enhancement of about 1.37 dB, 2 dB, 4.5 dB and 6.1 dB, after employing the (2×1), (2×2), (4×2) and (4×4) arrangements, respectively.

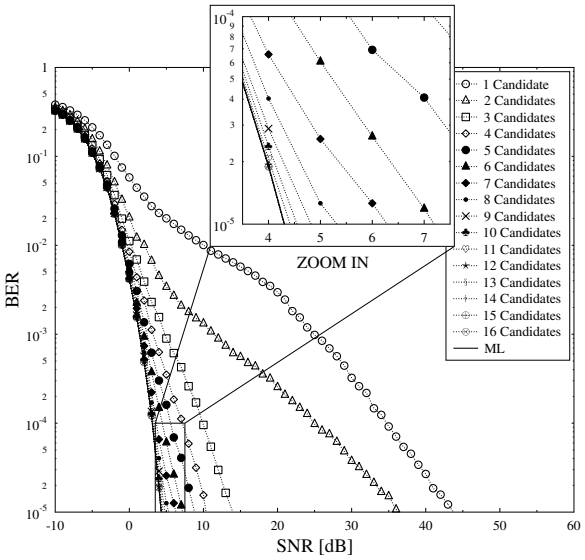

Figure 11. Achievable BER performance of our uncoded CS-aided STSK-IM system associated with an STSK(2, 2, 1, BPSK) encoder as well as N_f =8, N_a =16 and K =2 configurations based on the SFI technique, which relies on our RC-aided detector having J =1,. . . ,16 candidates.

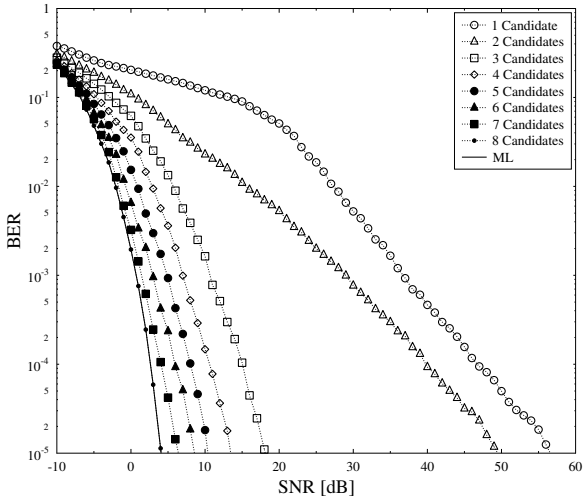

Figure 12. Achievable BER performance of our uncoded CS-aided STSK-IM system associated with an STSK(2, 2, 1, BPSK) encoder as well as N_f =8, N_a =16 and K =2 configurations based on the DFI technique, which relies on our RC-aided detector having J =1,. . . ,8 candidates.

Next, we investigate the BER performance of the RC-aided detection system associated with the SFI and DFI arrangements, as shown in Figure 11 and Figure 12, respectively. More specifically, we characterize the achievable BER performance of our uncodded CS-aided STSK-IM system associated with SFI and DFI, where they both employ an STSK(2, 2, 1, BPSK) encoder as well as the N_f =8, N_a =16 and K =2 configurations using J =1,. . . ,16 candidates for SFI and J =1,. . . ,8 for DFI, when employing the HD-aided RC technique discussed in Section II-D. The figures show that as the number of candidates increases, the BER performance of both systems approaches the performance of the optimum ML detector. In particular, observe that the J =6 BER curve seen in Figure 11 is close to that of the ML detection.

Finally, Figure 13 shows the achievable BER performance of the same system as used in Figure 11 relying on the RC-aided detector having J =4 and J =8 candidates, but using the SD-aided Aprox-Log-MAP detection technique presented in Section II-D. Observe in Figure 13 that the BER degradation of the system associated with J =4 can be overcome by introducing the iterative structure of Figure 1.

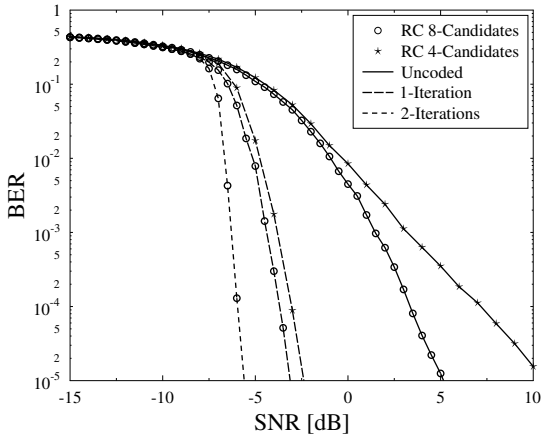

Figure 13. Achievable BER performance of our RSC-coded CS-aided STSK-IM system associated with an STSK(2, 2, 1, BPSK) encoder as well as N_f =8, N_a =16 and K =2 configurations based on the SFI technique, which relies on our RC-aided detector having J =4 and 8 candidates.

V. Conclusions

We commence by designing of our CS-aided STSK-IM scheme for mmWave communications. Then, we introduced both the optimum ML and the RC-aided detectors, which have a reduced complexity order of $\mathcal{O}\left(N_c \cdot (Q \cdot \mathcal{L})^K\right)$ to $\mathcal{O}\left(\hat{N}_c \cdot (Q \cdot \mathcal{L})^K\right)$, where $\hat{N}_c \leq N_c$. We also formulated the DCMC capacity of the system, where the CS-aided system exhibits a higher capacity than its counterpart using no CS. Next, we proposed a pair of sub-carrier allocation techniques and invoked EXIT charts for evaluating their capacities. Finally, we characterized the BER performance of our uncoded and coded systems employing both the

SFI and DFI techniques. We observed in Figure 9 that the BER performance of the system has significantly improved by CS. Our simulation results demonstrated that as the number of candidates invoked by the RC detector increases, the BER performance approaches that of the optimum detector upon increasing the complexity order. Furthermore, the coded systems showed a considerable BER improvement by mitigating the effect of choosing a low number of candidates for the RC-aided detector.

REFERENCES

[1] I. Hemadeh, K. Satyanarayana, M. El-Hajjar, and L. Hanzo, "Millimeter-Wave Communications: Physical Channel Models, Design Considerations, Antenna Constructions and Link-Budget," *IEEE Communications Surveys Tutorials*, vol. PP, no. 99, pp. 1–1, 2018.

[2] M. Agiwal, A. Roy, and N. Saxena, "Next Generation 5G Wireless Networks: A Comprehensive Survey," *IEEE Communications Surveys Tutorials*, vol. 18, no. 3, pp. 1617–1655, thirdquarter 2016.

[3] M. Shafi, A. F. Molisch, P. J. Smith, T. Haustein, P. Zhu, P. D. Silva, F. Tufvesson, A. Benjebbour, and G. Wunder, "5G: A Tutorial Overview of Standards, Trials, Challenges, Deployment, and Practice," *IEEE Journal on Selected Areas in Communications*, vol. 35, no. 6, pp. 1201–1221, June 2017.

[4] S. Kutty and D. Sen, "Beamforming for Millimeter Wave Communications: An Inclusive Survey," *IEEE Communications Surveys Tutorials*, vol. 18, no. 2, pp. 949–973, Secondquarter 2016.

[5] I. A. Hemadeh, P. Botsinis, M. El-Hajjar, S. Won, and L. Hanzo, "Reduced-RF-Chain Aided Soft-Decision Multi-Set Steered Space-Time Shift-Keying for Millimeter-Wave Communications," *IEEE Access*, vol. 5, pp. 7223–7243, 2017.

[6] E. Basar, M. Wen, R. Mesleh, M. D. Renzo, Y. Xiao, and H. Haas, "Index Modulation Techniques for Next-Generation Wireless Networks," *IEEE Access*, vol. 5, pp. 16 693–16 746, 2017.

[7] P. Yang, M. D. Renzo, Y. Xiao, S. Li, and L. Hanzo, "Design Guidelines for Spatial Modulation," *IEEE Communications Surveys and Tutorials*, vol. 17, no. 1, pp. 6–26, First Quarter 2015.

[8] I. A. Hemadeh, M. El-Hajjar, S. Won, and L. Hanzo, "Multi-Set Space-Time Shift-Keying With Reduced Detection Complexity," *IEEE Access*, vol. 4, pp. 4234–4246, 2016.

[9] E. Basar, U. Aygolu, E. Panayirci, and H. V. Poor, "Orthogonal Frequency Division Multiplexing With Index Modulation," *IEEE Transactions on Signal Processing*, vol. 61, no. 22, pp. 5536–5549, Nov 2013.

[10] R. Mesleh, H. Elgala, and H. Haas, "Optical Spatial Modulation," *IEEE/OSA Journal of Optical Communications and Networking*, vol. 3, no. 3, pp. 234–244, March 2011.

[11] B. Shamasundar, S. Jacob, S. Bhat, and A. Chockalingam, "Multidimensional Index Modulation in Wireless Communications," *CoRR*, vol. abs/1702.03250, 2017. [Online]. Available: http://arxiv.org/abs/1702.03250

[12] C. Sacchi, T. Rahman, I. A. Hemadeh, and M. El-Hajjar, "Millimeter-Wave Transmission for Small-Cell Backhaul in Dense Urban Environment: A Solution based on MIMO-OFDM And Space-Time Shift Keying (STSK)," *IEEE Access*, vol. 5, no. 99, pp. 4000–4017, 2017.

[13] K. Satyanarayana, M. El-Hajjar, P. H. Kuo, A. Mourad, and L. Hanzo, "Adaptive Transceiver Design for C-RAN in mmWave Communications," *IEEE Access*, vol. PP, no. 99, pp. 1–1, 2017.

[14] ——, "Dual-Function Hybrid Beamforming and Transmit Diversity Aided Millimeter Wave Architecture," *IEEE Transactions on Vehicular Technology*, vol. PP, no. 99, pp. 1–1, 2017.

[15] I. A. Hemadeh, M. El-Hajjar, S. Won, and L. Hanzo, "Multiuser Steered Multiset Space-Time Shift Keying for Millimeter-Wave Communications," *IEEE Transactions on Vehicular Technology*, vol. 66, no. 6, pp. 5491–5495, June 2017.

[16] A. Younis, N. Serafimovski, R. Mesleh, and H. Haas, "Generalised Spatial Modulation," Nov 2010.

[17] E. Basar, U. Aygolu, E. Panayirci, and H. Poor, "Space-Time Block Coded Spatial Modulation," *IEEE Transactions on Communications*, vol. 59, no. 3, pp. 823–832, March 2011.

[18] A. Younis, N. Abuzgaia, R. Mesleh, and H. Haas, "Quadrature Spatial Modulation for 5G Outdoor Millimeter-Wave Communications: Capacity Analysis," *IEEE Transactions on Wireless Communications*, vol. 16, no. 5, pp. 2882–2890, May 2017.

[19] N. Valliappan, A. Lozano, and R. Heath, "Antenna Subset Modulation for Secure Millimeter-Wave Wireless Communication," *IEEE Transactions on Communications*, vol. 61, no. 8, pp. 3231–3245, August 2013.

[20] P. Yang, Y. Xiao, Y. L. Guan, Z. Liu, S. Li, and W. Xiang, "Adaptive SM-MIMO for mmWave Communications With Reduced RF Chains," *IEEE Journal on Selected Areas in Communications*, vol. 35, no. 7, pp. 1472–1485, July 2017.

[21] E. Ozturk, E. Basar, and H. A. Cirpan, "Generalized Frequency Division Multiplexing with Index Modulation," in *IEEE Globecom Workshops (GC Wkshps)*, Dec 2016, pp. 1–6.

[22] S. Sugiura, S. Chen, and L. Hanzo, "Coherent and Differential Space-Time Shift Keying: A Dispersion Matrix Approach," *IEEE Transactions on Communications*, vol. 58, no. 11, pp. 3219–3230, November 2010.

[23] I. A. Hemadeh, M. El-Hajjar, S. Won, and L. Hanzo, "Layered Multi-Group Steered Space-Time Shift-Keying for Millimeter-Wave Communications," *IEEE Access*, vol. 4, pp. 3708–3718, 2016.

[24] Y. Liu, Z. Qin, M. Elkashlan, Z. Ding, A. Nallanathan, and L. Hanzo, "Nonorthogonal multiple access for 5g and beyond," *Proceedings of the IEEE*, vol. 105, no. 12, pp. 2347–2381, Dec 2017.

[25] P. Botsinis, I. Hemadeh, D. Alanis, Z. Babar, H. Nguyen, D. Chandra, S. X. Ng, M. El-Hajjar, and L. Hanzo, "Joint-Alphabet Space Time Shift Keying in mm-Wave Non-Orthogonal Multiple Access," *IEEE Access*, vol. PP, no. 99, pp. 1–1, 2017.

[26] I. A. Hemadeh, M. El-Hajjar, S. Won, and L. Hanzo, "Multi-Set Space-Time Shift Keying and Space- Frequency Space-Time Shift Keying for Millimeter-Wave Communications," *IEEE Access*, vol. 5, pp. 8324–8342, 2017.

[27] J. W. Choi, B. Shim, Y. Ding, B. Rao, and D. I. Kim, "Compressed Sensing for Wireless Communications: Useful Tips and Tricks," *IEEE Communications Surveys Tutorials*, vol. 19, no. 3, pp. 1527–1550, thirdquarter 2017.

[28] E. Basar, "OFDM With Index Modulation Using Coordinate Interleaving," *IEEE Wireless Communications Letters*, vol. 4, no. 4, pp. 381–384, Aug 2015.

[29] H. F. Schepker, C. Bockelmann, and A. Dekorsy, "Efficient Detectors for Joint Compressed Sensing Detection and Channel Decoding," *IEEE Transactions on Communications*, vol. 63, no. 6, pp. 2249–2260, June 2015.

[30] W. U. Bajwa, J. Haupt, A. M. Sayeed, and R. Nowak, "Compressed Channel Sensing: A New Approach to Estimating

Sparse Multipath Channels," *Proceedings of the IEEE*, vol. 98, no. 6, pp. 1058–1076, June 2010.

[31] H. Zhang, L. L. Yang, and L. Hanzo, "Compressed Sensing Improves the Performance of Subcarrier Index-Modulation-Assisted OFDM," *IEEE Access*, vol. 4, pp. 7859–7873, 2016.

[32] C. Xu, S. Sugiura, S. X. Ng, P. Zhang, L. Wang, and L. Hanzo, "Two Decades of MIMO Design Tradeoffs and Reduced-Complexity MIMO Detection in Near-Capacity Systems," *IEEE Access*, vol. 5, pp. 18 564–18 632, 2017.

[33] M. El-Hajjar and L. Hanzo, "EXIT Charts for System Design and Analysis," *IEEE Communications Surveys Tutorials*, vol. 16, no. 1, pp. 127–153, First 2014.

[34] M. Kadir, S. Sugiura, S. Chen, and L. Hanzo, "Unified MIMO-Multicarrier Designs: A Space-Time Shift Keying Approach," *Communications Surveys Tutorials, IEEE*, vol. 17, no. 2, pp. 550–579, Secondquarter 2015.

[35] D. L. Donoho, "Compressed sensing," *IEEE Transactions on Information Theory*, vol. 52, no. 4, pp. 1289–1306, April 2006.

[36] L. Hanzo, T. Liew, and B. Yeap, *Turbo Coding, Turbo Equalisation and Space-Time Coding for Transmission over Fading Channels*. Wiley, 2002. [Online]. Available: http://books.google.co.uk/books?id=3mOhrvMWTwQC

[37] D. J. Love and R. W. Heath, "Equal Gain Transmission In Multiple-Input Multiple-Output Wireless Systems," *IEEE Transactions on Communications*, vol. 51, no. 7, pp. 1102–1110, July 2003.

[38] J. Choi, "Sparse Index Multiple Access for Multi-carrier Systems with Precoding," *Journal of Communications and Networks*, vol. 18, no. 3, pp. 439–445, June 2016.

[39] S. X. Ng and L. Hanzo, "On The MIMO Channel Capacity Of Multidimensional Signal Setss," *IEEE Transactions on Vehicular Technology*, vol. 55, no. 2, pp. 528–536, March 2006.